

An analytic toy model for relativistic accretion in Kerr spacetime

Emilio Tejada^{1*}, Paul A. Taylor^{2*} and John C. Miller^{3,1*}

¹ *SISSA & INFN, Via Bonomea 265, 34136, Trieste, Italy*

² *Department of Radiology, UMDNJ-New Jersey Medical School, ADMC 5, Suite 575, 30 Bergen St., Newark, NJ 07103, USA*

³ *Department of Physics (Astrophysics), University of Oxford, Keble Road, Oxford OX1 3RH, UK*

9th September 2021

ABSTRACT

We present a relativistic model for the stationary axisymmetric accretion flow of a rotating cloud of non-interacting particles falling onto a Kerr black hole. Based on a ballistic approximation, streamlines are described analytically in terms of timelike geodesics, while a simple numerical scheme is introduced for calculating the density field. A novel approach is presented for describing all of the possible types of orbit by means of a single analytic expression. This model is a useful tool for highlighting purely relativistic signatures in the accretion flow dynamics coming from a strong gravitational field with frame-dragging. In particular, we explore the coupling due to this between the spin of the black hole and the angular momentum of the infalling matter. Moreover, we demonstrate how this analytic solution may be used for benchmarking general relativistic numerical hydrodynamics codes by comparing it against results of smoothed particle hydrodynamics simulations for a collapsar-like setup. These simulations are performed first for a ballistic flow (with zero pressure) and then for a hydrodynamical one where we measure the effects of pressure gradients on the infall, thus exploring the extent of applicability of the ballistic approximation.

Key words: accretion, accretion discs, black hole physics, relativity

1 INTRODUCTION

Matter falling down the potential well of a gravitating object is the fundamental mechanism behind some of the most powerful astrophysical phenomena in the universe (see e.g. Frank et al. 2002). The more compact the central object, the deeper into the well the matter can reach, and so the greater the quantity of potential energy available for extraction. However, for black holes (BHs), the most compact objects in the universe, purely radial infall is inefficient at converting kinetic energy into radiation since there is no resisting surface at which decelerate the infalling gas (Shapiro 1974). Traditionally, rotation of the accreting matter has been invoked (and also observed) as the means for providing, at least temporarily, centrifugal support to give time for different dissipative processes to take place and release part of the binding energy in the form of radiation. Gas rotation can lead to the formation of a disc-like structure (Prendergast & Burbidge 1968) and, indeed, accretion discs around BHs are the most commonly studied engines for explaining astrophysical phenomena such as active galactic nuclei

(Genzel et al. 2010), X-ray binaries (King 1995) and gamma-ray bursts (GRBs) (Piran 2004), and they may be produced as a possible outcome of tidal disruptions (Rosswog et al. 2009) and binary coalescence (Lee et al. 2010). Comprehensive analyses of these systems require full-scale, numerical magnetohydrodynamic simulations in a curved spacetime, together with an accurate microphysical description of the dissipative processes, such as cooling and shock formation. Nevertheless, typically two ingredients play the leading roles in determining the overall accretion efficiency: the gravitational field generated by the central BH and rotation of the fluid. An examination of the combination of these last two features is the focus of the present study.

Regarding the gravitational field, it has also been recognised that, in any realistic scenario, the central BH will possess some amount of intrinsic angular momentum, either because it was born with it or as a result of accretion of matter with large angular momentum (Bardeen 1970; Blandford 1987). Therefore, for applications in which it is safe to neglect the surrounding mass-energy contribution to the overall spacetime curvature, the exterior metric around a physical BH will be well approximated by the Kerr solution. Any substantial value for the angular momentum of the BH will significantly affect the innermost region of an accre-

* E-mail: tejeda@sissa.it (ET); ptaylor@astro.ox.ac.uk (PT); jcm@astro.ox.ac.uk (JCM).

tion disc around the BH, exactly where one expects to find the highest densities, temperatures and luminosities. For instance, the inner radius of a Keplerian-like accretion disc around a maximally rotating BH is around six times closer to the central accretor than it would be for a non-rotating BH (see e.g. Novikov & Thorne 1973), while the binding energy for the innermost stable circular orbit increases from $\sim 5.7\%$ of the rest-mass energy for a non-rotating BH up to $\sim 42\%$ for a maximally rotating one. This increase in both the surface area of the emitting disc and the binding energy released can substantially boost the overall efficiency of the system. Moreover, the BH angular momentum may play a relevant role in launching and accelerating a jet via e.g. the Blandford-Znajek mechanism (Blandford & Znajek 1977) and might also exert a torque on an accretion disc which happens to be tilted with respect to the BH rotation axis (Bardeen & Petterson 1975).

The present work constitutes a follow-up to the analytic accretion model introduced within a Newtonian framework by Mendoza et al. (2009) and for a Schwarzschild spacetime by Tejada et al. (2012) (referred to in the following as Paper I). Here we extend the general relativistic results of Paper I to a Kerr spacetime. Our aim in this series of papers has been to construct a toy model for the infall feeding an accretion disc around a BH, based solely on the two leading ingredients determining the fluid bulk motion: gravity and rotation. The model is based on the assumptions of stationarity, axisymmetry and ballistic motion, i.e. we assume that the fluid particles follow geodesic lines and neglect any deviation from their free-falling trajectories due to pressure gradients, magnetic fields, self-gravity, radiative processes, etc. It is clear that these assumptions constitute an oversimplification of the real situation but they allow us to give a useful analytic description of the streamlines and velocity field of the resulting flow. In addition, this will enable us to highlight the signatures of pure relativistic effects in the accretion dynamics, due to either the strong gravitational field or frame dragging, that might be otherwise masked by a fully hydrodynamic treatment. Our analytic description of the streamlines is based on the extensive body of work on geodesic motion already existing in the literature (see e.g. Sharp 1979; Chandrasekhar 1983, and references therein). Nevertheless, by using some standard identities for Jacobi elliptic functions, we provide here a novel approach for writing the solution for the radial and latitudinal motion of a timelike geodesic in Kerr spacetime in terms of a single analytic expression.

There are several interesting astrophysical systems where the accretion regimes are reasonably well approximated by the special conditions of the toy model. For instance, Beloborodov & Illarionov (2001); Kumar et al. (2008) and Zalamea & Beloborodov (2009) used a ballistic description for the infall feeding an accretion disc around a newly-formed BH, following the collapse of a massive star in the so-called collapsar scenario (Woosley 1993). Kumar et al. (2008) described the infall within Newtonian theory while Beloborodov & Illarionov (2001) and Zalamea & Beloborodov (2009) made general relativistic studies, first for a Schwarzschild BH and then for a Kerr one. These last two works were mainly focused on numerically solving for the structure of the disc and predicting a luminosity profile for the neutrino emission, while the infall was described ap-

proximately, considering parabolic-like energies for the incoming particles and restricting the analysis to boundary conditions with homogeneous density and small, uniform rotation rates. On the other hand, full-hydrodynamic numerical simulations for the collapsar scenario were performed by Lee & Ramírez-Ruiz (2006); López-Cámara et al. (2009) and Taylor et al. (2011). For some of the simulations presented in those works, a fairly stationary regime is reached where the infalling matter is not deviating significantly from free-fall in a large fraction of the spatial domain of the simulation, but a shock front develops around the accretion disc which abruptly decelerates the incoming streamlines and marks the transition from an essentially ballistic regime to a hydrodynamical one (see Paper I for a comparison with one of the collapsar models in Lee & Ramírez-Ruiz 2006). In those cases the present analytic model might be a valuable tool for describing the infalling matter which feeds the accretion disc, thereby enabling the exploration, in a computationally efficient manner, of a wide range of (often uncertain) boundary conditions (e.g. rotation profile, accretion rates) before performing full-scale numerical simulations.

In the present work we show comparisons between our analytic solutions and a series of 3D smoothed particle hydrodynamics (SPH) simulations made using a version of the publicly available code GADGET-2 (Springel 2005), modified by Taylor et al. (2011) to include a simplified treatment of neutrino cooling and to account for approximated general relativistic effects related to the Kerr metric by using the second-order expansion pseudo-Newtonian potential developed by Mukhopadhyay & Misra (2003). The purpose of this comparison was twofold. Firstly, we wanted to show the utility of the toy model as a simple, practical test for numerical codes which include dynamical effects of general relativity. Simulation results for pure ballistic motion (with the hydrodynamic forces being zeroed) can be directly and quantitatively compared with exact general relativistic results so as to test implementations of time-stepping algorithms, pseudo-Newtonian potentials, etc. Secondly, once the numerical features of particle motion within the simulation have been determined, one can then re-implement the hydrodynamic features within the code to investigate the effects of fluid flow behaviour, such as pressure, cooling and back-reaction from the accretion disc, on the particle trajectories. This second point can be viewed as an exploration of the validity of the ballistic approximation for describing the infall, showing the utility of the toy model itself for understanding a wide variety of astrophysical scenarios in a relatively simple way.

The paper is organised as follows. The general setup of the model is described in Section 2, while in Section 3 the velocity field of the accretion flow is given in terms of first integrals of motion. An analytic description of the streamlines is given in Section 4 in terms of Jacobi elliptic functions. A simple numerical scheme for calculating the density field is presented in Section 5. Applications of the model for some particular boundary conditions are then described in Section 6 and compared against full-hydrodynamic simulations in Section 7. Finally, a general discussion and our conclusions are presented in Section 8. Unless otherwise stated, we use geometrized units for which $c = G = 1$.

2 MODEL DESCRIPTION

In the present work we are constructing a model for the accretion flow of a rotating cloud of non-interacting particles towards a Kerr BH of mass M and specific angular momentum a . The model is based on the assumptions of stationarity and axisymmetry. We denote the constant accretion rate by \dot{M} (we are using the dot to represent differentiation with respect to proper time τ). In order to describe the overall accretion flow we adopt the Boyer-Lindquist (BL) system of coordinates (t, r, θ, ϕ) . The metric line element then has the familiar form (Misner et al. 1973)

$$ds^2 = - \left(1 - \frac{2Mr}{\rho^2}\right) dt^2 - \frac{4aMr \sin^2 \theta}{\rho^2} dt d\phi + \frac{\rho^2}{\Delta} dr^2 + \rho^2 d\theta^2 + \frac{\Sigma \sin^2 \theta}{\rho^2} d\phi^2, \quad (2.1)$$

where

$$\rho^2 = r^2 + a^2 \cos^2 \theta, \quad \Delta = r^2 - 2Mr + a^2, \quad (2.2)$$

$$\Sigma = (r^2 + a^2)^2 - a^2 \Delta \sin^2 \theta.$$

Considering a set of non-interacting particles means, in practice, that we are making a ballistic treatment of the fluid flow and hence that the accretion dynamics are solely determined by the gravitational field of the BH. Under the ballistic approximation, it is convenient to describe the whole gas cloud as a collection of equal-mass test particles. We take as the boundary of our model a ‘spherical’¹ shell at $r = r_0$ from which test particles are continuously injected. The infalling particles end up being either incorporated into an infinitesimally thin equatorial disc or directly accreted inside the BH horizon (located at $r_+ = M + \sqrt{M^2 - a^2}$). The analytic description of the infall does not include the disc itself where clearly a ballistic treatment is no longer valid; we shall just consider both disc and BH as passive sinks of particles and energy. We take the particle properties at r_0 to be given by specified distribution functions:

$$n_0 = n(r_0, \theta_0), \quad (2.3)$$

$$\dot{r}_0 = \dot{r}(r_0, \theta_0), \quad (2.4)$$

$$\dot{\theta}_0 = \dot{\theta}(r_0, \theta_0), \quad (2.5)$$

$$\dot{\phi}_0 = \dot{\phi}(r_0, \theta_0), \quad (2.6)$$

where n is the particle number density (as measured in a co-moving reference frame) and \dot{r} , $\dot{\theta}$, $\dot{\phi}$ are the radial, polar and azimuthal components of the four-velocity, respectively.

We require the four distribution functions in Eqs. (2.3)-(2.6) to be differentiable and symmetric with respect to the equatorial plane. Additionally, in order to avoid streamlines intersecting before they reach the equatorial plane, two further conditions need to be fulfilled. First, we require that the test particles do not have turning points in their polar or radial motion as they descend towards the equatorial plane. Second, we require the mapping $\theta_0 \rightarrow \theta$ to be non-singular, i.e.

$$\left. \left(\frac{\partial \theta}{\partial \theta_0} \right) \right|_r \geq 0. \quad (2.7)$$

¹ A surface $r = \text{const.}$ in Kerr spacetime (in BL coordinates) defines a spheroid with cross section $(\sqrt{r^2 + a^2} \sin \theta, r \cos \theta)$ in the R - z plane (see Eqs. 6.5 and 6.6).

A sufficient condition for satisfying Eq. (2.7) for a large fraction of the spatial domain is that the angular momentum distribution in the initial shell should increase monotonically towards the equatorial plane. For initial inward radial velocities above a certain threshold value, neighbouring streamlines are found to intersect each other in the immediate vicinity of the accretion disc. However the caustic surface defined by these intersections remains close to the equatorial plane in a region where the ballistic approximation is no longer expected to be valid (the existence of this detached caustic surface is also found in the Newtonian context as described in Mendoza et al. 2009).

3 VELOCITY FIELD

Within the ballistic approximation, streamlines of the accretion flow correspond to timelike geodesics in Kerr spacetime. Consider a test particle freely falling towards the central BH with four-velocity $u^\mu = \dot{x}^\mu$. The stationarity and axisymmetry of the Kerr metric lead to the existence of four first integrals of the motion which will enable us to describe the velocity field of the accretion flow (for a detailed derivation of the constants of motion, see Carter 1968). From the conservation of rest mass, one has as a first conserved quantity the four-velocity modulus given as

$$u^\mu u_\mu = -1. \quad (3.1)$$

The other three constants of motion are: E , the total specific energy; ℓ , the projection of the specific angular momentum on to the BH rotation axis; and Q , the Carter constant. Using BL coordinates, these quantities are given by

$$E = \left(1 - \frac{2Mr}{\rho^2}\right) \dot{t} + \frac{2aMr \sin^2 \theta}{\rho^2} \dot{\phi}, \quad (3.2)$$

$$\ell = -\frac{2aMr \sin^2 \theta}{\rho^2} \dot{t} + \frac{\Sigma \sin^2 \theta}{\rho^2} \dot{\phi}, \quad (3.3)$$

$$Q = \rho^4 \dot{\theta}^2 + \ell^2 \cot^2 \theta - \varepsilon a^2 \cos^2 \theta, \quad (3.4)$$

where, for convenience, we have introduced

$$\varepsilon = E^2 - 1. \quad (3.5)$$

Once the boundary conditions in Eqs. (2.3)-(2.6) have been fixed, the conserved quantities in Eqs. (3.2)-(3.4) are completely determined. Nonetheless, note that in general the conserved quantities will be functions of the initial polar angle θ_0 and, hence, vary from streamline to streamline. The value of \dot{t}_0 is calculated from Eq. (3.1) as a function of \dot{r}_0 , $\dot{\theta}_0$ and $\dot{\phi}_0$. Making use of the four integrals of motion, one gets the following system of equations determining the proper time evolution of the coordinates of the particle:

$$\rho^2 \frac{dr}{d\tau} = \pm \sqrt{\mathcal{R}}, \quad (3.6)$$

$$\rho^2 \frac{d\theta}{d\tau} = \pm \sqrt{\Theta}, \quad (3.7)$$

$$\rho^2 \frac{d\phi}{d\tau} = \frac{\mathcal{A}}{\sin^2 \theta} + a\mathcal{B}, \quad (3.8)$$

$$\rho^2 \frac{dt}{d\tau} = a\mathcal{A} + \mathcal{B}(r^2 + a^2), \quad (3.9)$$

where

$$\mathcal{R} = \varepsilon r^4 + 2Mr^3 + (\varepsilon a^2 - \ell^2 - Q)r^2 + 2M [Q + (aE - \ell)^2]r - a^2Q, \quad (3.10)$$

$$\Theta = Q + \varepsilon a^2 \cos^2 \theta - \ell^2 \cot^2 \theta, \quad (3.11)$$

$$\mathcal{A} = \ell - aE \sin^2 \theta, \quad (3.12)$$

$$\mathcal{B} = [E(r^2 + a^2) - a\ell] / \Delta. \quad (3.13)$$

The signs in Eqs. (3.6) and (3.7) are independent of each other and change whenever the test particle reaches a turning point in its trajectory (though, recall that in the present scenario, the radial coordinate has been required to decrease monotonically as the particle approaches the equatorial plane). Regarding the polar motion, since we have assumed mirror symmetry with respect to the equatorial plane, we can consider without loss of generality that the particle on which we are focusing is in, say, the northern hemisphere, i.e. $0 < \theta_0 < \pi/2$. For such a particle the polar coordinate increases from θ_0 to $\pi/2$. We then take the minus sign in Eq. (3.6) and the plus sign in Eq. (3.7).

In Eqs. (3.6)-(3.9), we already have expressions for the four components of the velocity field:

$$u^r = -\frac{\sqrt{\mathcal{R}}}{\rho^2}, \quad (3.14)$$

$$u^\theta = \frac{\sqrt{\Theta}}{\rho^2}, \quad (3.15)$$

$$u^\phi = \frac{\mathcal{A} + a\mathcal{B} \sin^2 \theta}{\rho^2 \sin^2 \theta}, \quad (3.16)$$

$$u^t = \frac{a\mathcal{A} + \mathcal{B}(r^2 + a^2)}{\rho^2}. \quad (3.17)$$

Eqs. (3.14)-(3.17) represent velocities with respect to the BL coordinate system as opposed to physical, locally measured ones. In order to get a local description of the velocity field, we follow Bardeen et al. (1972) and introduce a set of locally non-rotating frames (LNRFs). Associated with each LNRF there is an orthonormal tetrad of four-vectors constituting a local Minkowskian coordinate set of basis vectors. If we denote with a bar coordinates with respect to this local reference frame, the corresponding physical three-velocity field is given by

$$V^{\bar{r}} = -\frac{\sqrt{\mathcal{R}/\Delta}}{\gamma \rho}, \quad (3.18)$$

$$V^{\bar{\theta}} = \frac{\sqrt{\Theta}}{\gamma \rho}, \quad (3.19)$$

$$V^{\bar{\phi}} = \frac{\rho \ell}{\gamma \sqrt{\Sigma} \sin \theta}, \quad (3.20)$$

where γ is the Lorentz factor between the LNRF and the test particle passing by, and is given by

$$\gamma = \sqrt{1 + \frac{\mathcal{R}}{\Delta \rho^2} + \frac{\Theta}{\rho^2} + \frac{\rho^2 \ell^2}{\Sigma \sin^2 \theta}}. \quad (3.21)$$

Note that both sets of expressions for the velocity field (Eqs. 3.14 - 3.17 and Eqs. 3.18 - 3.20) are functions of the position (r, θ) as well as of the conserved quantities along each streamline, which have been determined by the initial position (r_0, θ_0) . Therefore, to use them in practice we need to provide an explicit mapping from $(r_0, \theta_0) \mapsto (r, \theta)$. Such

a mapping will be given in the next section in terms of an expression for the streamlines.

4 STREAMLINES

In this section we give an analytic solution for the radial and latitudinal motion of test particles freely falling in Kerr spacetime. It is not within the scope of the present work to give an exhaustive discussion of the qualitative features of the trajectories. For a thorough discussion of timelike geodesics around a rotating BH, see Wilkins (1972); Bardeen (1973); Chandrasekhar (1983); Dymnikova (1986); Frolov & Novikov (1998); Kraniotis (2004); Fujita & Hikida (2009); Grossman et al. (2012), while an in-depth analysis of the latitudinal and radial motion is given by de Felice & Calvani (1972); Bičák & Stuchlík (1976). In the following, we build on these previous works and give a novel approach for expressing the radial and latitudinal solutions of timelike geodesic motion by means of a single analytical formula.

Given the assumptions of stationarity and axisymmetry, all that is needed for completely describing a streamline of the present model is to consider the projection of an arbitrary timelike geodesic onto the r - θ plane. For doing this, it is sufficient to consider Eqs. (3.6) and (3.7) and to combine them in the following way

$$\int_{r_0}^r \frac{dr'}{\sqrt{\mathcal{R}(r')}} = - \int_{\theta_0}^\theta \frac{d\theta'}{\sqrt{\Theta(\theta')}}. \quad (4.1)$$

The solutions to both sides of the above equation can be expressed in terms of elliptic integrals (see e.g. Byrd & Friedman 1954). Let us introduce the following definitions:

$$\Phi(r) = \int_{r_a}^r \frac{dr'}{\sqrt{\mathcal{R}(r')}}}, \quad (4.2)$$

$$\Psi(\theta) = \int_{\theta_a}^\theta \frac{d\theta'}{\sqrt{\Theta(\theta')}}}, \quad (4.3)$$

where r_a and θ_a are as yet unspecified reference points in the particle trajectory. With these definitions we can rewrite Eq. (4.1) as

$$\Phi(r) - \Phi(r_0) = \Psi(\theta_0) - \Psi(\theta). \quad (4.4)$$

In the following, we give explicit expressions for $\Phi(r)$ and $\Psi(\theta)$.

4.1 Radial solution

Consider first Eq. (4.2). The procedure for solving this integral is technically the same as in the Schwarzschild case (see Paper I), with the solution depending on the nature of the roots of $\mathcal{R}(r)$. The physical interpretation of these roots is clear: whenever they are real and greater than r_+ , they constitute turning points of the radial motion at which \dot{r} changes sign and the direction of integration for the radial integral reverses. In the following, we briefly review the results of Wilkins (1972) and Dymnikova (1986) concerning the properties of the roots of $\mathcal{R}(r)$.

Since $\mathcal{R}(r)$ is a fourth order polynomial, there are the following possibilities for the roots: all four are real; two are real while the other two form a complex conjugate pair; there are two pairs of complex conjugates. The first two cases

include the possibility of multiplicity of the real roots. Although one can express the roots analytically in terms of the parameters of the orbit (E , ℓ and Q) (see e.g. Abramowitz & Stegun 1970), we do not give the final expressions coming from this here because we do not find them particularly useful in practice. Instead, we assume that we have already found the four roots, either analytically or by means of a root finding algorithm, and write $\mathcal{R}(r)$ as

$$\mathcal{R}(r) = \varepsilon(r - r_a)(r - r_b)(r - r_c)(r - r_d). \quad (4.5)$$

We label the roots in the following way:

(i) If $\mathcal{R}(r)$ has four real roots, and in order to satisfy the condition $\mathcal{R}(r) > 0$, there are two possibilities: either r is bracketed in between two non-negative consecutive roots of $\mathcal{R}(r)$, or r has a lower bound and is unbounded above. The latter case represents an open orbit with the largest positive root being the only turning point.

In the first case, we call the roots bracketing r , r_a and r_b (with $r_a < r_b$). In the second case we again take r_a as the lower bound for r and let r_b be the negative root with the largest absolute value. In both cases the two remaining roots are denoted as r_c and r_d (with $|r_c| < |r_d|$).

(ii) If $\mathcal{R}(r)$ has two real roots and a complex conjugate pair, we take r_a and r_d (with $|r_a| < |r_d|$) to be the real roots while r_b and r_c form the complex conjugate pair.

(iii) If $\mathcal{R}(r)$ has two complex conjugate pairs of roots, we take $r_b = r_c^*$ and $r_a = r_d^*$ with $\text{Re}(r_a) < \text{Re}(r_b)$. Note that this possibility is a special characteristic of Kerr spacetime, since in the Schwarzschild case one of the roots was zero and hence at least one other root was real as well.

With this way of labelling the roots, we can now express the radial solution as (Byrd & Friedman 1954)

$$\Phi(r) = \frac{2 \text{cn}^{-1} \left(\sqrt{\frac{(r_d - r_a)(r_b - r)}{(r_b - r_a)(r_d - r)}}, k_r \right)}{\sqrt{\varepsilon(r_a - r_c)(r_d - r_b)}}, \quad (4.6)$$

$$k_r = \sqrt{\frac{(r_b - r_a)(r_d - r_c)}{(r_d - r_b)(r_c - r_a)}}. \quad (4.7)$$

where $\text{cn}^{-1}(u, k_r)$ is the inverse of the Jacobi elliptic function $\text{cn}(\varphi, k_r)$ with modulus k_r . We refer interested readers to specialised literature on elliptic integrals (e.g. Hancock 1917; Cayley 1961; Lawden 1989) for a precise definition of Jacobi elliptic functions in terms of elliptic integrals.

In the cases (ii) and (iii), where complex roots arise, intermediate steps in the calculation of Eq.(4.6) involve the use of complex quantities, although the final result $\Phi(r) - \Phi(r_0)$ is always a real number. For alternative forms of the solution for the second and third cases, involving only explicitly real terms, see the Appendix.

Finally, we note that the solution for the radial motion in Eq.(4.6) is formally identical to the solution given in Paper I for a Schwarzschild spacetime.

4.2 Polar angle solution

We next consider Eq.(4.3). From that equation it is clear that the latitudinal motion is restricted to those values of θ

such that $\Theta(\theta) \geq 0$. Just as in the radial case, the polar angle solution depends on the nature of the roots of the equation $\Theta(\theta) = 0$. Whenever these roots belong to the natural domain of θ , i.e. $\theta \in [0, \pi]$, they constitute turning points of the polar motion at which $\dot{\theta}$ changes sign. These roots are straightforward to obtain after noticing that the equation $\Theta(\theta) = 0$ is equivalent to the following quadratic polynomial equation in $\cos^2 \theta$

$$\varepsilon a^2 \cos^4 \theta + (Q + \ell^2 - \varepsilon a^2) \cos^2 \theta - Q = 0. \quad (4.8)$$

Let θ_a be the turning point of the polar motion closest to the polar axis. For $\ell \neq 0$, θ_a corresponds to the smallest positive root of Eq.(4.8), and in this case it is convenient to rewrite Q in terms of θ_a as

$$Q = \ell^2 \cot^2 \theta_a - \varepsilon a^2 \cos^2 \theta_a. \quad (4.9)$$

In general, the polar equation $\Theta(\theta) = 0$ will have zero, two or four real roots in the interval of interest. The first case arises when $\ell = 0$ and $Q > -\varepsilon a^2$, corresponding to a test particle sweeping the whole polar domain and periodically crossing the polar axis.² The second case corresponds to bounded polar motion, $\theta \in [\theta_a, \pi - \theta_a]$, with the test particle periodically crossing the equatorial plane. The third case corresponds to a test particle restricted to move within a single hemisphere (in this case the northern one) as $\theta \in [\theta_a, \theta_b]$, where $\theta_b \leq \pi/2$ is the second turning point of the polar motion.

As follows from Eqs.(3.6) and (3.7), the polar and radial motions are decoupled, and hence their turning points are in general independent of each other. Since we have assumed that the particle starts its journey from the northern hemisphere, we have $\theta_a \leq \theta_0 \leq \pi/2$.

In terms of the angle θ_a , the solution for the polar integral is given by (Byrd & Friedman 1954)

$$\Psi(\theta) = \frac{\cos \theta_a}{\sqrt{Q}} \text{cd}^{-1} \left(\frac{\cos \theta}{\cos \theta_a}, k_\theta \right), \quad (4.10)$$

$$k_\theta = \sqrt{-\varepsilon a^2 / Q} \cos^2 \theta_a, \quad (4.11)$$

where $\text{cd}^{-1}(u, k_\theta)$ is the inverse of the Jacobi elliptic function $\text{cd}(\varphi, k_\theta)$ with modulus k_θ .

Note that $\Psi(\theta_a) = 0$, while for $\theta = \pi/2$

$$\Psi(\pi/2) = \frac{\cos \theta_a}{\sqrt{Q}} K(k_\theta), \quad (4.12)$$

where $K(k_\theta)$ is the complete elliptic integral of the first kind.

Just as in the radial case, for some values of the parameters ε and Q , intermediate steps in the computation of Eq.(4.10) might involve the use of complex quantities but the final result is always a real quantity. See the Appendix for alternative expressions for the polar solution involving just real quantities.

For the non-rotating BH case ($a = 0$) one gets $k_\theta = 0$ from Eq.(4.11). On the other hand, for a null value of the modulus, one has that $\text{cd}(\varphi, 0) = \cos(\varphi)$, and therefore in this case Eq.(4.10) can be simplified as

$$\Psi(\theta) = \frac{\cos \theta_a}{\sqrt{Q}} \cos^{-1} \left(\frac{\cos \theta}{\cos \theta_a} \right), \quad (4.13)$$

² Even though in this case the angles $\theta = 0, \pi$ do not satisfy $\Theta(\theta) = 0$, they still represent turning points since at those locations the polar velocity changes sign discontinuously. When this happens, we take $\theta_a = 0$.

which is the same expression as that found in Paper I (following a different approach).

4.3 Timelike geodesics

Bringing together the results in Eqs. (4.7) and (4.10), we arrive at the following expression for the projection onto the r - θ plane of a timelike geodesic in Kerr spacetime:

$$r = \frac{r_b(r_d - r_a) - r_d(r_b - r_a)\text{cn}^2(\xi, k_r)}{r_d - r_a - (r_b - r_a)\text{cn}^2(\xi, k_r)}, \quad (4.14)$$

with

$$\xi = \frac{\sqrt{\varepsilon(r_a - r_c)(r_d - r_b)}}{2} [\Phi(r_0) + \Psi(\theta_0) - \Psi(\theta)]. \quad (4.15)$$

Eqs. (4.14) and (4.15) constitute the analytic expression for the streamline of a gas element being accreted from (r_0, θ_0) .

5 DENSITY FIELD

In order to get a formal expression for calculating the density field, we start from the continuity equation

$$(n u^\mu)_{;\mu} = 0, \quad (5.1)$$

where a semi-colon denotes covariant differentiation. We integrate the above expression over a four-volume element \mathcal{V} , consisting of a streamline tube extending for an infinitesimal interval of coordinate time dt . We take the spatial cross-section of this streamline tube to be the collection of all of the streamlines starting to fall-in from a differential area element $dx^2|_{r_0}$ at the initial shell and ending up at a second sphere with arbitrary radius $r < r_0$. Denoting by $\partial\mathcal{V}$ the hypersurface delimiting the integrating volume and invoking the Gauss theorem, we have that

$$\int_{\mathcal{V}} (n u^\mu)_{;\mu} \sqrt{-g} d^4x = \oint_{\partial\mathcal{V}} n u^\mu N_\mu \sqrt{|h|} d^3x = 0, \quad (5.2)$$

where N_μ is a unit vector normal to $\partial\mathcal{V}$ and h is the determinant of the induced metric on this hypersurface. Since we have assumed stationarity, it is clear that the net particle flux through any closed spatial hypersurface at a given time t equals zero. Moreover, for the remaining mixed time-space hyperfaces of $\partial\mathcal{V}$, the contraction $u^\mu N_\mu$ will be, by construction, different from zero just for a hypersurface oriented perpendicularly to the radial direction. Hence, we have that Eq. (5.2) reduces to

$$n u^\mu N_\mu^{(r)} \sqrt{|h^{(r)}|} dt d\theta d\phi \Big|_r^{r_0} = 0. \quad (5.3)$$

Substituting into this equation that $N_\mu^{(r)} = \delta_\mu^r / \sqrt{g^{rr}}$ where $g^{rr} = \Delta/\rho^2$, together with $h^{(r)} = \Delta\rho^2 \sin^2\theta$, we arrive at

$$n u^r \rho^2 \sin\theta dt d\theta d\phi \Big|_r^{r_0} = 0. \quad (5.4)$$

Invoking once again the stationarity and axisymmetry conditions, it follows that $dt_0 d\phi_0 = dt d\phi$. Using this result in Eq. (5.4) allows us to solve for n , getting

$$n = \frac{n_0 u_0^r \rho_0^2 \sin\theta_0}{u^r \rho^2 \sin\theta} \left(\frac{\partial\theta}{\partial\theta_0} \right)^{-1}. \quad (5.5)$$

Just as in the Schwarzschild case, analytically calculating the partial derivative in Eq. (5.5) would be a rather involved process, whereas evaluating it numerically is a trivial task. We refer the reader to Paper I for a description of a numerical scheme for computing n .

The requirement that there should be no early intersections of streamlines before the equator has been reached (see Eq. 2.7) ensures that the expression for calculating the density in Eq. (5.5) is well defined.

6 APPLICATIONS OF THE ANALYTIC MODEL

We now illustrate our analytic model by applying it to an example scenario with boundary conditions consisting of matter in uniform rotation on a uniform shell, i.e.:

$$n_0 = \text{const.}, \quad (6.1)$$

$$\dot{r}_0 = \text{const.}, \quad (6.2)$$

$$\dot{\phi}_0 = \text{const.}, \quad (6.3)$$

$$\dot{\theta}_0 = 0. \quad (6.4)$$

The condition in Eq. (6.4) implies that, for every streamline, $\theta_a = \theta_0$.

Figure 1 shows six panels with the streamlines, velocity field and density contours for six different combinations of the flow parameters. The panels consist of spatial projections onto the R - z plane, where R and z (together with θ) are the cylindrical coordinates associated with the BL ones and are defined as

$$R = \sqrt{r^2 + a^2} \sin\theta, \quad (6.5)$$

$$z = r \cos\theta. \quad (6.6)$$

For specifying the set of model parameters in each case, we have used a , r_0 , V_e^r and V_e^ϕ , where the subscript e indicates that the corresponding quantity is being evaluated at the equator of the shell. Note that, for the present boundary conditions, the set of parameters $(a, r_0, V_e^r, V_e^\phi)$ has a one-to-one correspondence with $(a, r_0, \dot{r}_0, \dot{\phi}_0)$ given by the inversion of the system of Eqs. (3.18)-(3.21). Also note that fixing this set of parameters specifies a family of models rather than a single one, since both length and density scales can still be arbitrarily and independently chosen.

The radius of the outer edge of the disc being formed, r_D , measured as the outermost material first reaches the equatorial plane, can be calculated from Eq. (4.15), taking first $\theta = \pi/2$ and then $\theta_0 = \pi/2$, giving

$$\xi_D = \frac{\sqrt{\varepsilon(r_a - r_c)(r_d - r_b)}}{2} \left[\Phi(r_0) - \frac{\pi}{2\sqrt{\ell_e^2 - \varepsilon a^2}} \right], \quad (6.7)$$

and then substituting the result into Eq. (4.14).

In Figure 2, we have plotted r_D , first as a function of the BH spin a and then as a function of the specific angular momentum at the equator of the shell, $\ell_e = \ell(\pi/2)$. Here we have assumed $V_e^\phi > 0$, and so a negative value of a implies a counter-rotating disc. From this figure we can clearly see how the BH spin couples with the angular momentum of the disc (through the frame dragging effect), giving rise to a larger r_D for a co-rotating disc and a smaller r_D for a counter-rotating one. It is also clear that, as intuitively expected, r_D is a monotonically increasing function of both V_e^ϕ and V_e^r .

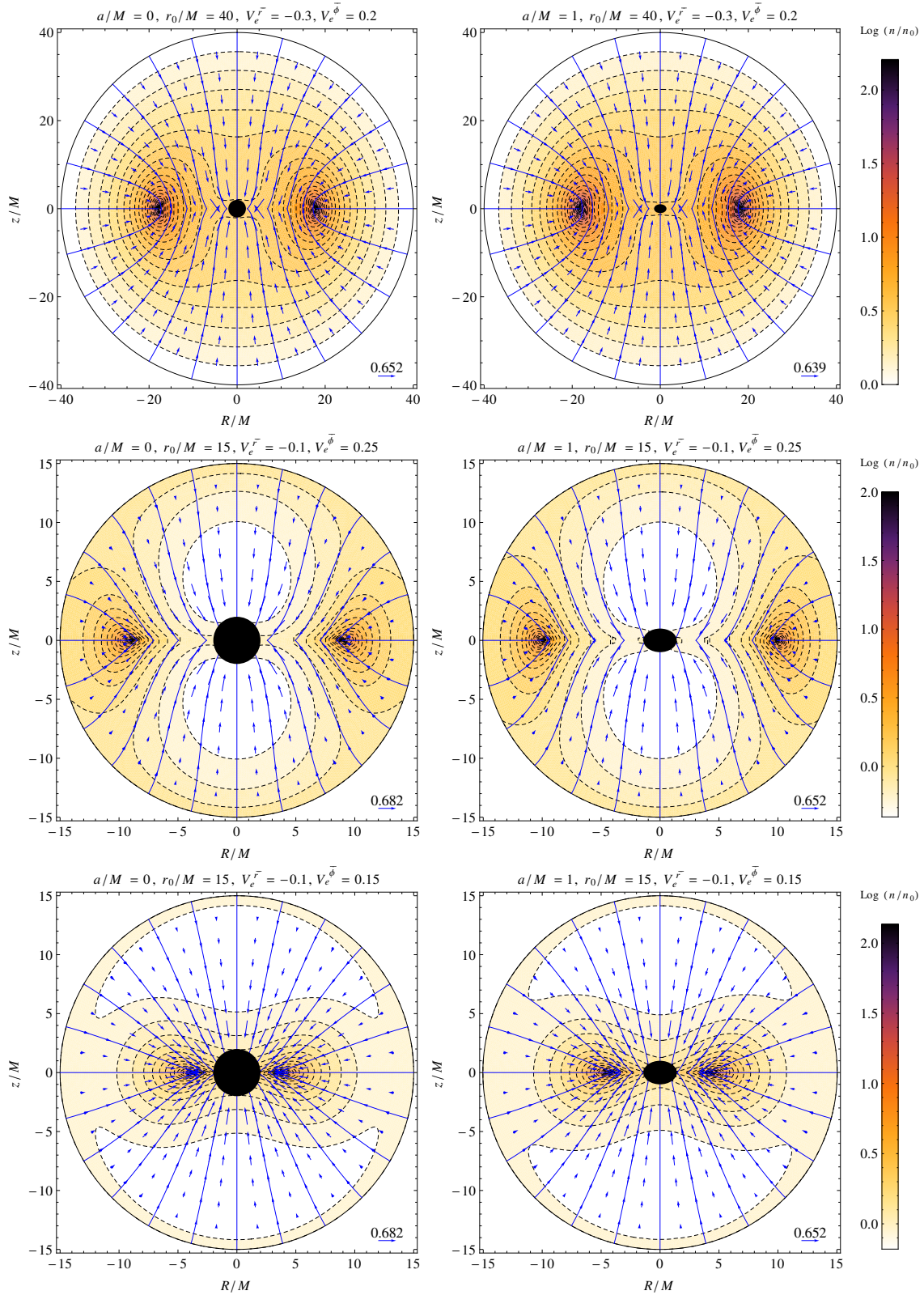


Figure 1. Streamlines, velocity field and density contours for six different combinations of the flow parameters. The values of the parameters used in each case are indicated above each panel. Each panel shows the spatial projection onto the R - z plane and the colour coding corresponds to the value of the logarithm of the particle number density $\text{Log}(n/n_0)$, with the scale being indicated by the colour-coding bar at the left of each row. The arrows correspond to the V^r and V^θ components of the velocity field. The magnitude of the largest arrow is indicated at the bottom right of each panel.

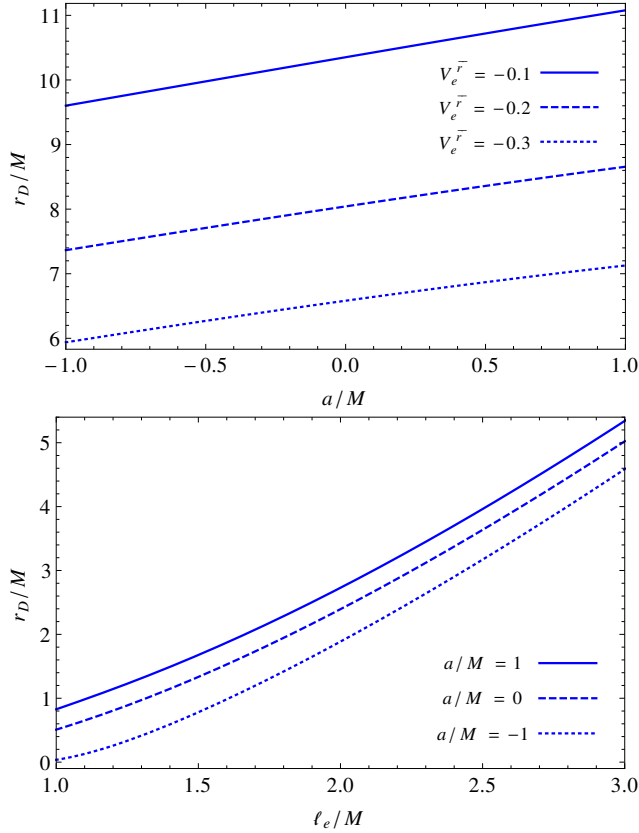


Figure 2. Plot of r_D versus a (top panel) and r_D versus ℓ_e (bottom panel). In the top panel, fixed values are taken for $r_0 (= 20M)$ and $V_e^{\bar{\phi}} (= 0.2)$ while in the bottom panel, fixed values are taken for $r_0 (= 60M)$ and $V_e^{\bar{r}} (= -0.2)$. Note how the BH spin couples with the angular momentum of the infalling matter and leads to a larger r_D for a co-rotating flow and to a smaller r_D for a counter-rotating one.

Working with the LNRF velocities $V_e^{\bar{r}}$ and $V_e^{\bar{\phi}}$ makes the exploration of the parameter space easier since, being physical velocities, they are naturally bounded as $V_e^{\bar{r}} \in (-1, 0]$ and $V_e^{\bar{\phi}} \in [0, 1)$. Furthermore, for fixed values of r_0 and a , a pair of velocities in the $V_e^{\bar{r}}-V_e^{\bar{\phi}}$ plane is also restricted by the condition that the resulting r_D should satisfy $r_D \in (r_+, r_0)$. In Figure 3 we have plotted the regions on the velocity space which lead to an outer radius of the disc satisfying this criterion. The plot has been constructed for a fixed value of $r_0 = 10M$ and three different values of a . From this figure we observe that the domain of values in the velocity space leading to physically relevant accretion models shifts to smaller values of $V_e^{\bar{\phi}}$ as a increases. This behaviour is a consequence of the frame dragging effect: for a given test particle with fixed azimuthal velocity $V_e^{\bar{\phi}}$, its associated angular momentum is an increasing function of a , and hence points in the $V_e^{\bar{r}}-V_e^{\bar{\phi}}$ plane which, in the low- a case, did not have large enough angular momentum to keep the outer edge of the disc outside the event horizon, are able to do so for a larger value of a . Conversely, low- a models with an angular momentum only just small enough to form any disc inside their initial shell would have discs entirely outside their initial shell when a is increased (thus becoming excluded from the parameter domain). Also note that this parameter-space

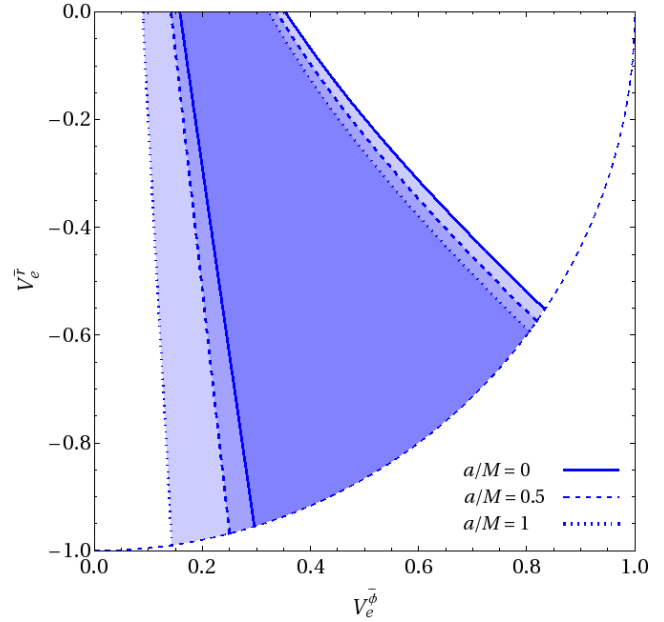


Figure 3. The pairs of velocity values $V_e^{\bar{r}}-V_e^{\bar{\phi}}$ leading to a disc radius such that $r_D \in [r_+, r_0]$ are plotted for a fixed value of $r_0 = 10M$ and for $a/M = 0, 0.5, 1$. The upper boundary for each value of a represents the points $(V_e^{\bar{r}}, V_e^{\bar{\phi}})$ such that $r_D = r_0$, while the lower one represents those such that $r_D = r_+$. Note how the domain of values in the velocity space leading to physically relevant accretion models shifts to smaller values of $V_e^{\bar{\phi}}$ as a increases, because of the frame-dragging effect.

effect is greater on the lower boundary of $V_e^{\bar{\phi}}$ than on the upper one, which is simply due to the fact that the frame dragging increases as $r \rightarrow r_+$.

7 COMPARISON WITH NUMERICAL SIMULATIONS

In this section we compare the analytic solution derived above against SPH simulations performed with the modified version of the code GADGET-2 (Springel 2005) presented and used by Taylor et al. (2011). In that work, the authors studied numerically the production of the progenitors for long-duration GRBs as the aftermath of the collapse of a massive star, starting off from realistic initial conditions and including cooling by neutrino emission. They also included a rough approximation of Kerr metric general relativistic effects by using the second-order expansion pseudo-Newtonian potential developed by Mukhopadhyay & Misra (2003) (MM). Note that, among the several different pseudo-Newtonian potentials that exist for mimicking effects of Kerr spacetime, the choice of MM was intended to roughly minimise the overall effect of errors in the approximation of various dynamic properties such as location of the innermost stable circular orbit, epicyclic frequencies and radial acceleration (for further discussion see the Appendix B of Taylor et al. 2011).

Here, we compare our ballistic toy model (calculated with the full Kerr metric) with results from various versions of the SPH code implementing approximate gravity prescriptions: in addition to the MM potential, we have also

experimented with the classical Newtonian potential and the widely-used pseudo-Newtonian potential of Paczyński & Wiita (1980) (PW). In connection with the two pseudo-Newtonian potentials, we should stress that they have been designed particularly for capturing relevant relativistic features of importance for accretion discs, including getting correct locations for the innermost stable circular orbit in Kerr and Schwarzschild spacetimes, respectively. This does not at all guarantee that they would be good for other purposes such as the infall calculations being discussed here. However, they have been widely used in more general contexts and so it is relevant for us to test them against the toy model.

In order to perform a systematic analysis in which we are able to distinguish between hydrodynamic and gravitational effects, we have considered two kinds of simulation:

(i) Ballistic free-fall, with the SPH particles being automatically removed when they cross either the equatorial plane or the BH horizon. Here we consider an equation of state (EoS) for which the fluid pressure $P = 0$, and hence, effectively ‘turn off’ the hydrodynamical forces. The aim of this kind of simulation is to highlight the differences in the flow dynamics coming from the use of different gravity descriptions (full general relativity, Newtonian gravity, and the MM and PW pseudo-Newtonian potentials) and from different numerical implementations of the equations of motion for the particles.

(ii) Full-hydrodynamical simulations, including back reaction from a growing equatorial disc and cooling in regions where the gas gets very hot ($\geq 10^9$ K). Here we do not remove SPH particles when they reach the equatorial plane but rather let them settle down by themselves into a disc structure. In this case we employ a polytropic EoS of the form $P = (\Gamma - 1) n u$, where n is the baryon number density, u the internal energy per baryon and Γ is the polytropic index. We take $\Gamma = 4/3$, and the value of the internal energy (taken to be constant in the initial shell) is set at an arbitrary but non-negligible value of one tenth of the sum of kinetic energy and absolute value of the Newtonian potential energy for an SPH particle at the equator of the shell, i.e. $u = 0.1 \left(\dot{r}_0^2/2 + r_0^2 \dot{\phi}_0^2/2 + M/r_0 \right)$.

For both types of simulation, we take stationary boundary conditions with SPH particles being continuously injected with constant density and velocity distributions from a fixed injection radius r_0 . We treat the BH horizon (located at r_+) as an inner boundary at which particles are extracted from the simulation. For a fair comparison with the toy model, we report here late-time snapshots of the simulations in which the system has evolved to a quasi-stationary state (at least in the region away from the disc). As mentioned above, the number of particles being used in these was continuously changing, but was around 2.5×10^5 at the time shown. Moreover, in order to reduce the noise level and exploiting the axisymmetry of the system, the results presented in the following were obtained after averaging over 24 cross-sectional $\phi = \text{const.}$ slices of the 3D simulations.

7.1 Example I

Here we consider a set of parameter values for the system that might arise in the context of collapsing stellar cores leading to long GRBs, namely

$$a = 0.5 M, \quad (7.1)$$

$$M = 4 M_\odot, \quad (7.2)$$

$$\dot{M} = 0.01 M_\odot/s, \quad (7.3)$$

$$r_0 = 100 M, \quad (7.4)$$

$$\dot{r}_0 = -1/\sqrt{50}, \quad (7.5)$$

$$r_0 \dot{\phi}_0 = 0.038, \quad (7.6)$$

$$\dot{\theta}_0 = 0. \quad (7.7)$$

Note that, for convenience, we have used standard (non-geometrized) units to express the total accretion rate in Eq. (7.3).

For this set of boundary conditions, we present in Figure 4 the analytic solution alongside the results of both the ballistic and polytropic simulations. The figure shows a spatial projection of each case onto the R - z plane with isodensity contours, streamlines and velocity fields. Let us focus first on the ballistic simulation result (middle panel), which rapidly reached a stationary state. In this figure we see an overall satisfactory agreement with the analytic solution, although a closer inspection of the streamlines reveals some quantitative differences. We also note that the simulation isodensity contours are somewhat ‘noisy’ compared with the analytic results. Nevertheless, this level of fluctuation is consistent with the effects of discretisation and interpolation within SPH simulations.

Figure 5 shows a closer comparison of the streamlines of the analytic solution with the ones of the ballistic simulation. Since hydrodynamical effects are absent in this case, the differences between the numerical simulation and the toy model can reasonably be attributed mainly to the different descriptions of gravity: Kerr spacetime against the MM pseudo-Newtonian potential. From this figure we see that the streamlines in the two cases deviate significantly from each other just for $r \lesssim 10 M$ and that far away from the central BH the differences between these two descriptions of gravity become negligible (bear in mind that the streamlines originate from $r = 100 M$).

We now investigate the inclusion of hydrodynamic properties of the flow by comparing the polytropic SPH simulation shown in the bottom panel of Figure 4 with the corresponding ballistic flow shown in the middle one. In Figure 6 we present a direct comparison of the streamlines for these two cases. The first important thing to note is that in the polytropic simulation, unlike in the ballistic one, SPH particles are not removed from the simulation at the equatorial plane and, therefore, the build-up of a disc can take place. This is indeed the case for the present set of parameter values, for which we observe a disc that keeps growing in mass and expands horizontally. The material in this disc corresponds to the fraction of the infalling matter which possesses enough angular momentum to remain in a stable orbit around the BH. Since it is not within the scope of the present article to study the evolution of such a disc, we show here a snapshot at a time at which any kind of initial transient related to the initial conditions has faded away, but, at the same time, neither the mass nor the extension of the

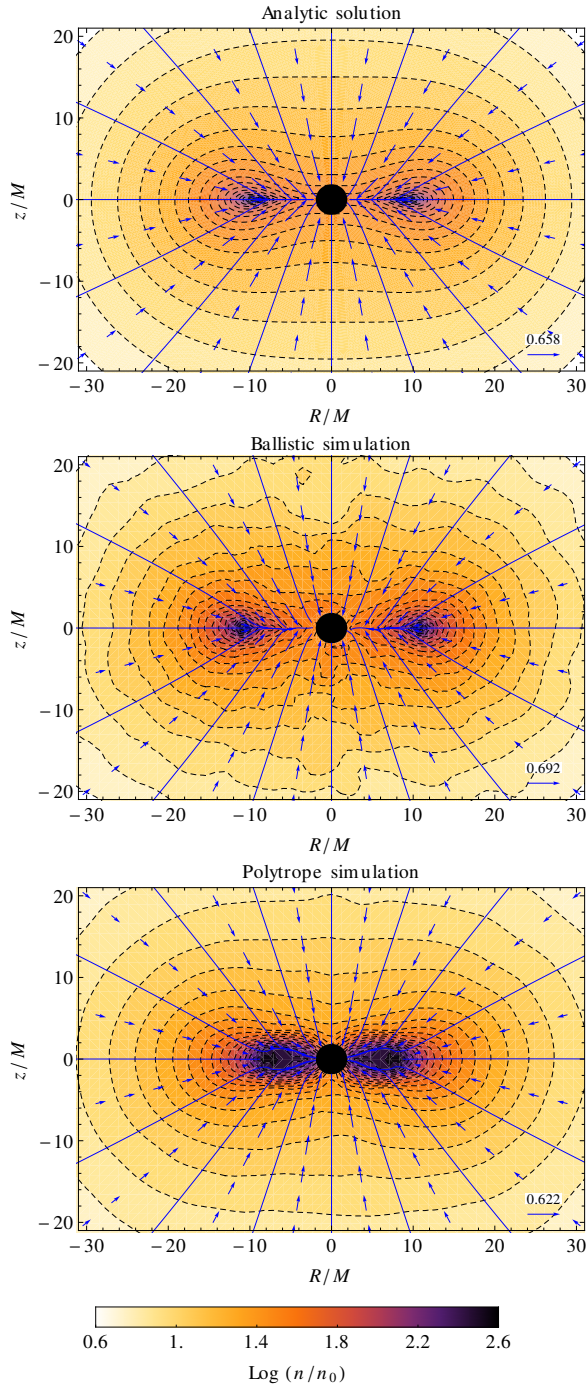


Figure 4. Isodensity contours, streamlines and velocity fields for the analytic solution and for the ballistic and polytropic SPH simulations, for an accretion flow onto a rotating BH with $a = 0.5 M$. The model parameters are as given in Eqs. (7.1)-(7.7). General relativistic effects in the SPH simulations are mimicked using the MM pseudo-Newtonian potential. The common scale for the density colour coding is shown at the bottom of the figure. The velocity field in each panel is represented by the two-vectors (V^R, V^z) ; the length scale for these vectors is given at the bottom right corner of each panel. The SPH simulations used a varying total particle number, but typically this was around 2.5×10^5 at the times shown (mass per SPH particle $\approx 3.6 \times 10^{-10} M_\odot$).

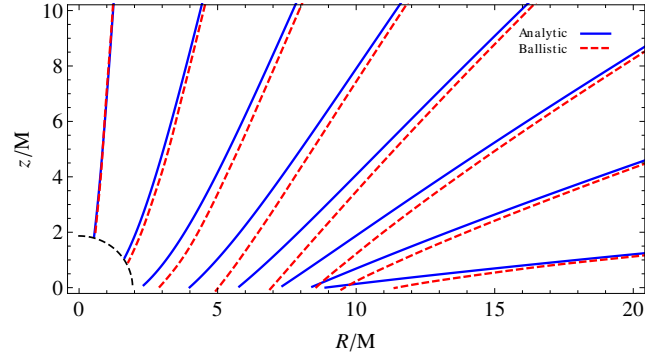


Figure 5. Streamlines corresponding to the analytic solution and to the ballistic SPH simulation for an accretion flow onto a rotating BH with $a = 0.5 M$ (see top and middle panels of Figure 4). General relativistic effects in the SPH simulation are here mimicked using the MM pseudo-Newtonian potential. The figure shows the first quadrant of the R - z plane with the BH horizon (located at r_+) indicated with a dashed-line quarter-circle.

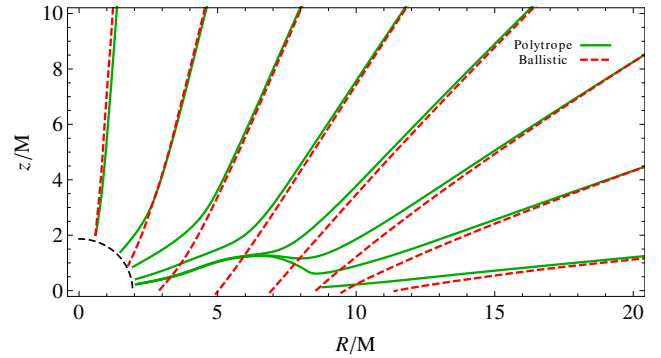


Figure 6. Streamlines corresponding to the ballistic and polytropic SPH simulations made with the MM pseudo-Newtonian potential for an accretion flow onto a rotating BH with $a = 0.5 M$ (see the middle and bottom panels of Figure 4). The figure shows a zoom-in of the first quadrant of the R - z plane. The BH horizon (located at r_+) is indicated with the dashed-line quarter-circle.

disc have grown importantly (additionally, the presence of cooling in the simulation aids in limiting the disc height).

A second important feature characterising the polytropic simulation is the existence of a shock front around the disc, marking the boundary between two different flow regimes. In the pre-shock region, a clear stationary regime is rapidly reached where the flow moves supersonically and is highly laminar. In this region, which we shall refer to as the infall region, we find that the polytropic simulation produces quite similar results to the ballistic one, and hence also to the toy model. On the other hand, in the post-shock region the flow is decelerated, the streamlines deviate away from the ballistic trajectories due to the action of pressure gradients and, in this way, are prevented from having a ‘head-on’ collision with their symmetric counterparts coming from the opposite hemisphere. Clearly, the full hydrodynamical evolution in this region will depend on the particular EoS being used as well as on the particular mechanism driving the accretion (e.g. viscosity, dynamical instabilities, etc.) and also the cooling prescription, but again, the details of this post-

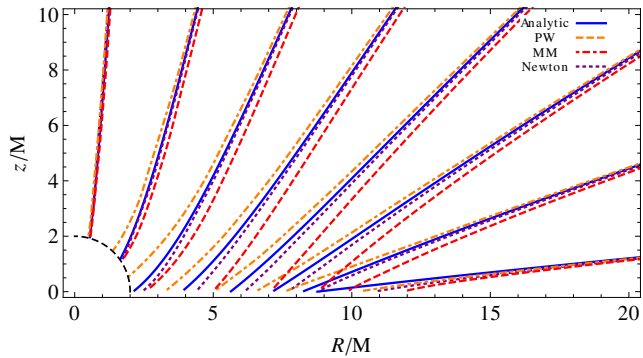


Figure 7. Streamlines corresponding to the analytic solution and to the three ballistic SPH simulations for a non-rotating BH ($a = 0$) with the remaining boundary conditions being as in Eqs. (7.2)-(7.7). The figure shows a zoom-in of the first quadrant of the R - z plane. The BH horizon (located at r_+ and which represents the inner boundary) is indicated with the dashed-line quarter-circle.

shock region were outside the scope of the present study. From Figure 4 we also note that the isodensity contours of the polytropic simulation in the infall region are less noisy than those of the ballistic simulation, due to the action of pressure forces in smoothing out the particle distribution and so reducing discretisation fluctuations.

Note that, in comparing Figures 5 and 6, the departure of the ballistic streamlines from the analytic solution occurs earlier and for a larger fraction of the simulation domain than the differences between the ballistic and polytropic streamlines. In other words we see that here, adopting an improved description for the gravitational field of the BH has a greater effect on the infall part of the simulation than including pressure.

7.2 Example II

In order to make a connection with the results presented in Paper I and to demonstrate the application of the toy model as a useful tool for studying the effect of different gravity treatments, we considered the same boundary conditions as in Eqs. (7.2)-(7.7) but now with $a = 0$. This same set of parameters was also used in Paper I to make a comparison with one of the GRB simulations of Lee & Ramírez-Ruiz (2006) using the PW potential.

Figure 7 shows a comparison of the analytic general relativistic streamlines with those coming from ballistic SPH simulations with the three different gravitational potentials: the classical Newtonian one, and the PW and MM pseudo-Newtonian ones. Note how the streamlines obtained with the Newtonian potential are closer to the general relativity solution than those obtained with the pseudo-Newtonian potentials. In this figure we can also see that the PW streamlines arrive at the equatorial plane at smaller radii than the analytic relativistic ones, while the Newtonian and MM ones arrive at larger radii. This suggests that equivalent hydrodynamical simulations implementing the PW potential would underestimate the extension of any resulting disc while those implementing the Newtonian and MM potentials would overestimate it.

Once more we analyse the role of pressure gradients on

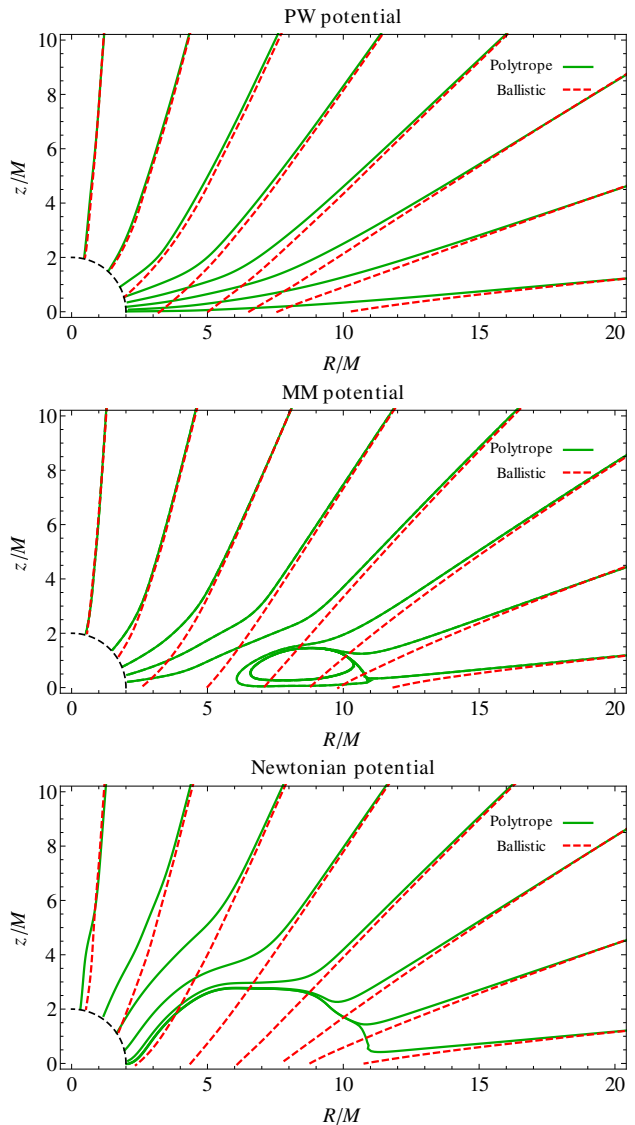


Figure 8. Comparison of the streamlines from SPH simulations for ballistic motion against those for a polytropic fluid. Note that only for the run using the PW potential does the resulting flow correspond to a ‘small-scale inviscid disc’. In the other two cases, the infalling matter keeps accumulating in a ring around the BH. This effect is more evident in the case with the MM potential.

the infall by showing in Figure 8 the results from polytropic simulations for the three potentials employed in Figure 7 in comparison with the equivalent ballistic ones. We see a quite good match between the two sets of streamlines in the infall region while the effects of the pressure gradients become significant only in the high density region near to the equatorial plane. Again, in this region we observe that a shock front develops around the disc where the incoming streamlines decelerate and deviate from the corresponding ballistic trajectories.

With respect to the $a \neq 0$ case in Section 7.1, the change in the spin parameter of the BH does not lead to significant differences in either the velocity field or the density field of the accretion flow in the infall region. Nevertheless, a crucial difference comes at the level of the long term evolution

of the resulting disc since, for the present boundary conditions with $a = 0$, one expects that none of the matter in the equatorial plane would possess enough angular momentum to maintain a stable orbit around the central BH and, hence, that all of the infalling material should be accreted into the BH on a dynamical time-scale. This kind of accretion corresponds to the ‘small-scale inviscid disc’ regime discussed by Beloborodov & Illarionov (2001). In this respect, an important difference among the accretion flows corresponding to different potentials is already apparent in Figure 8. In this figure we see that only the disc corresponding to the PW potential evolves as an accretion disc within the ‘small-scale inviscid disc’ regime (in which a stationary state is rapidly reached). For the other two cases we observe a growing ring of matter with enough angular momentum to avoid direct accretion onto the BH (even though the ballistic streamlines for the Newtonian potential appear to give the best match to those of the analytic relativistic solution in Figure 7); the resulting disc in each of these cases is then expected to evolve on a viscous time-scale rather than the much shorter dynamical time-scale.

8 DISCUSSION AND CONCLUSIONS

In this paper, we have presented an analytic toy model for the relativistic accretion of non-interacting particles onto a Kerr BH. Taking the assumptions of stationarity, axisymmetry and ballistic motion, we have given analytic expressions for the streamlines and the velocity fields as well as a simple numerical scheme for calculating the density field. This model is a generalisation of the one presented in Paper I for Schwarzschild spacetime, and it has been demonstrated how the earlier results are easily recovered from the present solution in the non-rotating limit.

Using a single analytic expression for describing the streamlines constitutes a novel way of expressing the solution to the latitudinal and radial motion of timelike geodesics in Kerr spacetime. The generality of this expression is shown in the Appendix by using standard identities of the Jacobi elliptic functions.

The conditions for the initial profiles of Eqs. (2.3)-(2.6) were differentiability and axisymmetry with respect to the equatorial plane. While these are very broad and applicable to a number of astrophysical situations, a further extension of these analytic expressions would be to include more asymmetric situations, such as an inhomogeneous density distribution or an overall rotation which is not aligned with the black hole angular momentum (occurring physically, for example, in the GRB case of a kick during an associated supernova). This is something that we plan to investigate in future work.

We have explored the effect of frame dragging on the resulting accretion flow and found that an effective coupling occurs between the BH spin and the angular momentum of the infall, leading to more extended discs if the flow is co-rotating with the BH and smaller discs in the counter-rotating case.

Our model allows for a fairly wide range of boundary conditions to be used, making it an ideal tool for exploring the effect of different flow parameters (accretion rates, angular momentum and density distributions, etc.) in ap-

plications where the approximations of steady-state and axisymmetry are reasonable ones. These assumptions are often met in some interesting astrophysical scenarios such as under-luminous accretion towards supermassive BHs, winded X-ray binaries and collapsars in which the accretion disc remains thin either due to efficient cooling or because it evolves within the ‘small-scale inviscid’ regime. In this paper we have shown a series of comparisons between the toy model and full-hydrodynamic, numerical simulations for a collapsar-like setup. Rather good agreement was obtained between the simulations and the toy model, under circumstances where one might expect to have agreement. The main discrepancies between the resulting accretion flows in the infall region have been shown to be related more to the different treatments of the gravitational field produced by the BH rather than to the ballistic description of the infall. Indeed, we observed that the effects of pressure gradients tend to become important just in the immediate proximity of the disc, where a shock front develops and decelerates the incoming flow. A new kind of exploratory simulation can be envisaged in which simple but general boundary conditions are set far away from the central object and then, by using the toy model, transported down to the region in which pressure gradients become dominant where a proper hydrodynamical study can then be performed. This kind of approach would greatly reduce the spatial domain of the simulation, allowing greater resolution and reducing the computing time.

Given the analytic nature of the present model, it provides a very practical tool for use in benchmarking general relativistic hydrodynamics codes and this, indeed, was the main motivation for the present work which forms part of a larger project for building a new general relativistic SPH code. Also, this toy model allows simple and direct comparisons between approximate methods for including general relativistic effects in simulations on a case-by-case basis. We have used it here to test the performance of SPH simulations implementing two pseudo-Newtonian potentials (MM and PW) and found good overall qualitative agreement between the toy model and the simulations, although we have also seen that apparently small quantitative discrepancies in the flows can eventually lead to rather different long-term evolutions. In the purely ballistic comparisons, we found good agreement between the trajectories coming from different gravity descriptions in the regions far away from the BH. However, as the test particles approach the inner region, the different trajectories start to deviate significantly from each other. How important these discrepancies are in practice will certainly depend on the particular application; nonetheless, from the present results we can conclude that neither of the two pseudo-Newtonian potentials considered here is particularly well suited for reproducing off-equatorial motion of test particles.

9 ACKNOWLEDGEMENTS

The authors thank Zdenek Stuchlík, Stephan Rosswog and Iván Zalamea for fruitful discussions, and Sergio Mendoza for initially motivating the study of this problem. We would also like to thank the anonymous referee for helpful suggestions and remarks.

References

- Abramowitz M., Stegun I., 1970, *Handbook of Mathematical Functions*. New York: Dover, 1970
- Bardeen J. M., 1970, *Nature*, 226, 64
- Bardeen J. M., 1973, in Dewitt, C. & Dewitt, B. S. eds., *Black Holes (Les Astres Occlus)*. Timelike and null geodesics in the Kerr metric. Gordon and Breach, New York, pp 215–239
- Bardeen J. M., Petterson J. A., 1975, *ApJL*, 195, L65
- Bardeen J. M., Press W. H., Teukolsky S. A., 1972, *ApJ*, 178, 347
- Beloborodov A. M., Illarionov A. F., 2001, *MNRAS*, 323, 167
- Bičák J., Stuchlík Z., 1976, *Bulletin of the Astronomical Institutes of Czechoslovakia*, 27, 129
- Blandford R. D., 1987, in Hawking, S. W. & Israel, W. eds., *Three Hundred Years of Gravitation*. Astrophysical black holes. Cambridge University Press, p. 277
- Blandford R. D., Znajek R. L., 1977, *MNRAS*, 179, 433
- Byrd P., Friedman M., 1954, *Handbook of elliptic integrals for engineers and physicists*. Springer-Verlag, Berlin
- Carter B., 1968, *Phys. Rev.*, 174, 1559
- Cayley A., 1961, *An elementary treatise on elliptic functions*. New York : Dover, 1961
- Chandrasekhar S., 1983, *The Mathematical Theory of Black Holes*. Oxford University, Oxford
- de Felice F., Calvani M., 1972, *Nuovo Cimento B Serie*, 10, 447
- Dymnikova I. G., 1986, *Soviet Physics Uspekhi*, 29, 215
- Frank J., King A., Raine D. J., 2002, *Accretion Power in Astrophysics: Third Edition*. Cambridge University Press
- Frolov V. P., Novikov I. D., 1998, *Black Hole Physics. Basic Concepts and New Developments*. Kluwer Academic, Dordrecht
- Fujita R., Hikida W., 2009, *Classical and Quantum Gravity*, 26, 135002
- Genzel R., Eisenhauer F., Gillessen S., 2010, *Rev. Mod. Phys.*, 82, 3121
- Grossman R., Levin J., Perez-Giz G., 2012, *Physical Review D*, 85, 023012
- Hancock H., 1917, *Elliptic Integrals*. New York : Dover, 1917
- King A., 1995, in Lewin, W. H. G., van Paradijs, J., & van den Heuvel, E. P. J. eds., *X-ray Binaries. Accretion in close binaries*. Cambridge University Press, p. 419
- Kraniotis G. V., 2004, *Classical and Quantum Gravity*, 21, 4743
- Kumar P., Narayan R., Johnson J. L., 2008, *MNRAS*, 388, 1729
- Lawden D. F., 1989, *Elliptic Functions and Applications*. Springer-Verlag, New York
- Lee W. H., Ramírez-Ruiz E., 2006, *ApJ*, 641, 961
- Lee W. H., Ramírez-Ruiz E., van de Ven G., 2010, *ApJ*, 720, 953
- López-Cámara D., Lee W. H., Ramírez-Ruiz E., 2009, *ApJ*, 692, 804
- Mendoza S., Tejada E., Nagel E., 2009, *MNRAS*, 393, 579
- Misner C. W., Thorne K. S., Wheeler J. A., 1973, *Gravitation*. San Francisco: W.H. Freeman and Co., 1973
- Mukhopadhyay B., Misra R., 2003, *ApJ*, 582, 347
- Novikov I. D., Thorne K. S., 1973, in Dewitt, C. & Dewitt, B. S. eds., *Black Holes (Les Astres Occlus)*. Astrophysics of black holes. Gordon and Breach, New York, pp 343–450
- Paczynsky B., Wiita P. J., 1980, *Astronomy and Astrophysics*, 88, 23
- Piran T., 2004, *Reviews of Modern Physics*, 76, 1143
- Prendergast K. H., Burbidge G. R., 1968, *ApJL*, 151, L83+
- Rosswog S., Ramírez-Ruiz E., Hix W. R., 2009, *ApJ*, 695, 404
- Shapiro S. L., 1974, *Astrophysical Journal*, 189, 343
- Sharp N. A., 1979, *General Relativity and Gravitation*, 10, 659
- Springel V., 2005, *MNRAS*, 364, 1105
- Taylor P. A., Miller J. C., Podsiadlowski P., 2011, *MNRAS*, 410, 2385
- Tejada E., Mendoza S., Miller J. C., 2012, *MNRAS*, 419, 1431
- Wilkins D. C., 1972, *Physical Review D*, 5, 814
- Woosley S. E., 1993, *BAAS*, 25, 894
- Zalamea I., Beloborodov A. M., 2009, *MNRAS*, 398, 2005

APPENDIX A: RADIAL AND LATITUDINAL MOTION

In Section 4 we have given analytic solutions for the radial and latitudinal motion of a timelike geodesic in Kerr spacetime. These expressions are general but involve the use of complex quantities in some cases. In this appendix we consider these special cases for both types of motion and, by means of standard identities for Jacobi elliptic functions (see e.g. Cayley 1961; Abramowitz & Stegun 1970), we rewrite the solutions when necessary in such a way that just real quantities are involved.

A1 Radial solution

Let us consider the solution to the radial integral in Eq. (4.2), i.e.

$$\int_{r_a}^r \frac{dr'}{\sqrt{\mathcal{R}(r')}} = \Phi(r). \quad (\text{A.1})$$

The general solution to Eq. (A.1) was given in Eq. (4.6). That expression involves the use of complex quantities when $\mathcal{R}(r)$ has complex roots and should be handled with care when $\varepsilon = 0$. In order to give alternative expressions for these cases, we consider the various possibilities one by one:

Case I: Four real roots

The labelling of the roots here proceeds as described in Section 4.1. In this case the solution given in Eq. (4.6) involves only the use of real quantities. For the sake of completeness, we reproduce it here

$$\Phi(r) = \frac{2 \operatorname{cn}^{-1} \left(\sqrt{\frac{(r_d - r_a)(r_b - r)}{(r_b - r_a)(r_d - r)}}, k_r \right)}{\sqrt{\varepsilon(r_a - r_c)(r_d - r_b)}}, \quad (\text{A.2})$$

$$k_r = \sqrt{\frac{(r_b - r_a)(r_d - r_c)}{(r_d - r_b)(r_c - r_a)}}. \quad (\text{A.3})$$

Case II: Two real roots and a complex conjugate pair

We have that r_a and r_d (with $r_a < |r_d|$) are the real roots while r_b and r_c form a complex conjugate pair. We define the following three real constants

$$\alpha = \operatorname{Sign}(\varepsilon) \sqrt{(r_d - r_b)(r_d - r_c)}, \quad (\text{A.4})$$

$$\beta = \sqrt{(r_a - r_b)(r_a - r_c)}, \quad (\text{A.5})$$

$$\tilde{k}_r^2 = \frac{(\alpha + \beta)^2 - (r_d - r_a)^2}{4\alpha\beta}. \quad (\text{A.6})$$

From the definition of k_r in Eq. (A.3), it is easy to check the following relation

$$\tilde{k}_r^2 = \frac{(1 + k_r)^2}{4k_r}. \quad (\text{A.7})$$

Now consider the following identity for Jacobi elliptic functions

$$\operatorname{cn} \left(2\sqrt{k} \varphi, \frac{1+k}{2\sqrt{k}} \right) = \frac{1 - k \operatorname{sn}^2(\varphi, k)}{1 + k \operatorname{sn}^2(\varphi, k)}. \quad (\text{A.8})$$

Defining $u = \operatorname{cn}(\varphi, k)$ and inverting Eq. (A.8) gives

$$\operatorname{cn}^{-1}(u, k) = \frac{1}{2\sqrt{k}} \operatorname{cn}^{-1} \left[\frac{1 - k(1 - u^2)}{1 + k(1 - u^2)}, \frac{1+k}{2\sqrt{k}} \right], \quad (\text{A.9})$$

from where, and after some algebra, we can rewrite $\Phi(r)$ in Eq. (A.2) as

$$\Phi(r) = \frac{1}{\sqrt{\varepsilon\alpha\beta}} \operatorname{cn}^{-1} \left[\frac{\beta r_d - \alpha r_a + (\alpha - \beta)r}{\beta r_d + \alpha r_a - (\alpha + \beta)r}, \tilde{k}_r \right], \quad (\text{A.10})$$

which is now an explicit real function of r .

Case III: Two pairs of complex conjugates

This case is a new possibility for Kerr spacetime that is not present in the Schwarzschild case since there one of the roots of $\mathcal{R}(r)$ is always zero and, therefore, there is at least one other real root (see Paper I).

We start by noting that, since $\Phi(r)$ is defined in Eq. (A.1) in terms of an integral with a complex number as its lower limit, $\Phi(r)$ is itself a complex function of r . In the following, we first split $\Phi(r)$ into its real and imaginary parts and then show that the latter is independent of r , and so $\Phi(r) - \Phi(r_0)$ will always be a real function of r .

According to the labelling of the roots in Section 4.1, in this case we have $r_a = r_d^*$ and $r_b = r_c^*$, with $\operatorname{Re}(r_a) < \operatorname{Re}(r_b)$. Also, it is simple to check that α and β , as defined in Eq. (A.4), now form a complex conjugate pair, i.e. $\alpha = \beta^*$. We then introduce the following real constants

$$\begin{aligned} \mu &= \frac{r_a + r_d}{2}, & \nu &= \frac{r_a - r_d}{2i}, \\ \zeta &= \frac{\alpha + \beta}{2}, & \eta &= \frac{\alpha - \beta}{2i}. \end{aligned} \quad (\text{A.11})$$

Using these definitions, it is simple to check that \tilde{k}_r , as defined in Eq. (A.6), can also be expressed as

$$\tilde{k}_r^2 = \frac{\zeta^2 + \nu^2}{\zeta^2 + \eta^2}, \quad (\text{A.12})$$

from which it is clear that \tilde{k}_r is still a real quantity. On the other hand, from Eq. (A.10) and the definitions in Eq. (A.11), it is simple to check that

$$\frac{\beta r_d - \alpha r_a + (\alpha - \beta)r}{\beta r_d + \alpha r_a - (\alpha + \beta)r} = i \frac{\zeta \nu - \eta(r - \mu)}{\eta \nu + \zeta(r - \mu)}, \quad (\text{A.13})$$

i.e. the argument of the function cn^{-1} in Eq. (A.10) is a pure imaginary number. Moreover, from Eq. (A.12) it follows that

$$\sqrt{\varepsilon\alpha\beta} \tilde{k}_r = \sqrt{\varepsilon(\zeta^2 + \nu^2)}. \quad (\text{A.14})$$

We now consider the following identity for Jacobi elliptic functions

$$\operatorname{cn}(\phi, k) = i \operatorname{cs} \left[k \phi + i K \left(1 + \frac{1}{k} \right), \frac{1}{k} \right], \quad (\text{A.15})$$

where K is the complete elliptic integral of the first kind. Again defining $u = \operatorname{cn}(\varphi, k)$ and solving for φ in Eq. (A.15) gives

$$\operatorname{cn}^{-1}(u, k) = \frac{1}{k} \left[\operatorname{cs}^{-1} \left(-i u, \frac{1}{k} \right) - i K \left(1 + \frac{1}{k} \right) \right]. \quad (\text{A.16})$$

Introducing $\tilde{\Phi}(r)$ as the following real function of r

$$\tilde{\Phi}(r) = \frac{1}{\sqrt{\varepsilon(\zeta^2 + \nu^2)}} \operatorname{cs}^{-1} \left[\frac{\zeta \nu - \eta(r - \mu)}{\eta \nu + \zeta(r - \mu)}, \frac{1}{\tilde{k}_r} \right], \quad (\text{A.17})$$

and combining Eqs. (A.13), (A.14), (A.16) and (A.17), it is simple to check that

$$\Phi(r) = \tilde{\Phi}(r) - \frac{i K \left(1 + \frac{1}{k} \right)}{\sqrt{\varepsilon(\zeta^2 + \nu^2)}}. \quad (\text{A.18})$$

This last equation explicitly splits $\Phi(r)$ into a real function of r and an imaginary constant. From this, it follows that

$$\Phi(r) - \Phi(r_0) = \tilde{\Phi}(r) - \tilde{\Phi}(r_0) \quad (\text{A.19})$$

is a real function of r .

Case IV: $\varepsilon = 0$

In this case we have that one of the roots diverges to infinity and so $\mathcal{R}(r)$ reduces to a third order polynomial. Here there are two possibilities for the roots: either the three of them are real, or one is real and the other two form a complex conjugate pair. Appropriate expressions for each case are straightforward to obtain from Eqs. (A.2) and (A.10) after taking the corresponding limit. See Paper I for an analogous procedure.

A2 Polar solution

We now return to the polar integration discussed in Section 4.2 and consider the polar solution as given in Eq. (4.10). That expression is always a real function of θ but, for some values of Q and ε , it might involve the use of complex quantities as intermediate steps. Here we show how to rewrite $\Psi(\theta)$ in a way which involves only real quantities. For doing this, we consider the following cases:

Case I: $\varepsilon \leq 0$

In this case, it follows from Eq. (4.9) that $Q \geq 0$ and so all of the quantities involved in Eq. (4.10) are real. For the sake of completeness, we reproduce the expression here

$$\Psi(\theta) = \frac{\cos \theta_a}{\sqrt{Q}} \text{cd}^{-1} \left(\frac{\cos \theta}{\cos \theta_a}, k_\theta \right), \quad (\text{A.20})$$

where

$$k_\theta = \sqrt{-\varepsilon a^2 / Q} \cos^2 \theta_a. \quad (\text{A.21})$$

Note that when $\varepsilon = 0$ then $k_\theta = 0$, and since $\text{cd}(\varphi, 0) = \cos(\varphi)$ then Eq. (A.20) can be simplified as

$$\Psi(\theta) = \frac{\cos \theta_a}{\sqrt{Q}} \cos^{-1} \left(\frac{\cos \theta}{\cos \theta_a} \right). \quad (\text{A.22})$$

As noted in Section 4.2, this result also follows when $a = 0$; hence Eq. (A.22) is the expression to use in Schwarzschild spacetime (see Paper I).

Case II: $\varepsilon > 0$ and $Q > 0$

Here one has that k_θ is a pure imaginary number. Using the following identity for Jacobi elliptic functions

$$\text{cd}(\varphi, k) = \text{cn} \left(\frac{\varphi}{\sqrt{1-k^2}}, \sqrt{\frac{-k^2}{1-k^2}} \right), \quad (\text{A.23})$$

one can rewrite $\Psi(\theta)$ in Eq. (A.20) as

$$\Psi(\theta) = \frac{\cos \theta_a}{\sqrt{Q + \varepsilon a^2 \cos^4 \theta_a}} \text{cn}^{-1} \left(\frac{\cos \theta}{\cos \theta_a}, \tilde{k}_\theta \right), \quad (\text{A.24})$$

with

$$\tilde{k}_\theta = \sqrt{\frac{-k_\theta^2}{1-k_\theta^2}} = \sqrt{\frac{\varepsilon a^2 \cos^4 \theta_a}{Q + \varepsilon a^2 \cos^4 \theta_a}}. \quad (\text{A.25})$$

Case III: $\varepsilon > 0$ and $Q \leq 0$

In this case, we use the identity

$$\text{cn}(\phi, k) = \text{dn}(k\phi, k^{-1}) \quad (\text{A.26})$$

to transform $\Psi(\theta)$ as written in Eq. (A.24) into

$$\Psi(\theta) = \frac{1}{\sqrt{\varepsilon} a \cos \theta_a} \text{dn}^{-1} \left(\frac{\cos \theta}{\cos \theta_a}, \frac{1}{\tilde{k}_\theta} \right). \quad (\text{A.27})$$

When $Q = 0$ then $\tilde{k}_\theta = 1$ and, since $\text{dn}(\varphi, 1) = \text{sech}(\varphi)$, Eq. (A.27) can be simplified as

$$\Psi(\theta) = \frac{1}{\sqrt{\varepsilon} a \cos \theta_a} \text{sech}^{-1} \left(\frac{\cos \theta}{\cos \theta_a} \right). \quad (\text{A.28})$$

Case IV: $\ell = 0$

In this case, the expressions in Eqs. (A.20), (A.24) and (A.27) can be used without further modification. Nevertheless, note that here one has the possibility of reaching the polar axis where the polar coordinate is singular. This happens when $\ell = 0$ and $Q > -\varepsilon a^2$, and in this case one should take $\theta_a = 0$ which, although it is not a formal root of the equation $\Theta(\theta) = 0$, does constitute a turning point of the polar motion since here one has that the polar velocity changes sign discontinuously every time that the particle crosses the polar axis.